The Astrophysical Journal, 999:266 (11pp), 2026 March 10 https://doi.org/10.3847/1538-4357/ae472c
© 2026. The Author(s). Published by the American Astronomical Society.
OPEN ACCESS

# Chromospheric Spectra of Small-scale Dynamic Features Observed on and off Solar Disk with Goode Solar Telescope

Vasyl Yurchyshyn[1], Seray Şahin[1,2], Anneliese Schmidt[1], Eun-Kyung Lim[3,4], Nicolas Gorceix[1], Xu Yang[1], and Wenda Cao[1]
[1] Big Bear Solar Observatory, New Jersey Institute of Technology, 40386 North Shore Lane, Big Bear City, CA 92314, USA
[2] Department of Space Sciences and Technologies, Akdeniz University Faculty of Science, 07058, Antalya, Türkiye
[3] Korea Astronomy and Space Science Institute, Daedeokdae-ro 776, Yuseong-gu, Daejeon 34055, Republic of Korea
[4] Astronomy and Space Science, University of Science and Technology, 217 Gajeong-ro, Yuseong-gu, Daejeon 34113, Republic of Korea
*Received 2025 July 31; revised 2026 February 11; accepted 2026 February 14; published 2026 March 9*

## Abstract

Our study of H$\alpha$ line profiles of rapid blue- and redshifted excursions measured with Goode Solar Telescope revealed an asymmetrical three-peak structure present in the blue wing of the H$\alpha$ line, suggesting complex internal velocity fields that may include bidirectional flows and transverse and torsional motions. Blueshifted plasma predominates across the field of view (FOV), correlating with higher temperatures ($>10^4$ K) and extending to greater heights. Conversely, redshifts are less spread over the FOV, are localized near network magnetic fields, and diminish rapidly with altitude. The frequency distribution associated with blueshifted events displays a bimodal structure with peaks centered at 7200 and 8800 K. The redshifted events display a much weaker and wide peak centered at about 9000 K. No significant difference in temperature distributions for blue- and redshifted events is observed in the range above 10,000 K. Variations of H$\alpha$ line profiles with height seem to indicate that the line-of-sight integration effects may be most significant within the 0–6 Mm layer above the photosphere, and it decreases with height.

*Unified Astronomy Thesaurus concepts:* Quiet sun (1322); Quiet solar chromosphere (1986); Solar spicules (1525)

## 1. Introduction

One of the most important questions in solar physics is why the solar corona is hotter than its underlying surface, known as the coronal heating problem. Magnetic reconnection and wave interaction are two mechanisms that can provide energy for coronal heating. Spicules, which are dynamic jetlike plasma structures observed in the solar chromosphere, are viable candidates for facilitating mass and energy transport from the chromosphere and transition region (TR) to the solar corona (e.g., L. Rouppe van der Voort et al. 2015; V. M. J. Henriques et al. 2016; J. Martínez-Sykora et al. 2017). Observed in chromospheric lines such as H$\alpha$ and Ca II, spicules are classified into two types (B. De Pontieu et al. 2007a). Type I spicules have been known for decades (e.g., see review by J. M. Beckers 1968). They tend to appear near strong magnetic fields (B. De Pontieu et al. 2004) and display upward and downward velocities of 10–30 km s$^{-1}$, reaching heights of 2–9 Mm (J. M. Beckers 1968). Type I spicules are typically found in active regions (ARs), exhibit behavior similar to dynamic fibrils, and are thought to be driven by magnetoacoustic waves or shocks (V. H. Hansteen et al. 2006).

Type II spicules were identified in early Hinode data (B. De Pontieu et al. 2007a) and are described as short-lived (<100 s), thin (<0.″7) structures observed everywhere on the solar disk in Hinode Ca II images. They show high upward Doppler velocities (50–150 km s$^{-1}$; B. De Pontieu et al. 2007a), as well as return flows (T. M. D. Pereira et al. 2014). When observed in Interface Region Imaging Spectrograph (IRIS) data, they show higher apparent speeds of 80–300 km s$^{-1}$ (H. Tian et al. 2014; N. Narang et al. 2016). They are primarily seen in areas distant from ARs, specifically in coronal holes and in quiet-Sun (QS) areas. V. L. Herde et al. (2023) conducted the first systematic survey of on-disk type II spicules using IRIS Mg II *h* and *k* line observations, revealing spicule occurrence peaks at locations with magnetic field strengths of 100–200 G, highlighting their role in chromospheric dynamics and coronal mass supply. Type II spicules are omnipresent and carry a large amount of magnetic energy (B. De Pontieu et al. 2007b, 2012; S. W. McIntosh et al. 2011; J. Liu et al. 2019); therefore, they might be related to the process of heating and replenishing the corona with hot plasma. They are often found to be heated rapidly to TR (T. M. D. Pereira et al. 2014; L. Rouppe van der Voort et al. 2015) and even coronal temperatures (B. De Pontieu et al. 2011; V. M. J. Henriques et al. 2016; S. Bose et al. 2025).

When observed on the solar disk, type II spicules were identified as blue- and red-shifted jetlike features termed by L. Rouppe van der Voort et al. (2009) as rapid blue- and redshifted excursions (RBEs and RREs). T. M. D. Pereira et al. (2012) performed comprehensive analysis of RBEs based on off-disk data measuring their lifetime (50–150 s) and the range of velocities (30–110 km s$^{-1}$). RBEs show measurable transverse displacement of 0.1–1.0 Mm, with the corresponding rates of 5–40 km s$^{-1}$ peaking at about 10 km s$^{-1}$. RBEs exhibit low inclination angles ranging from $-30°$ to 30° and peaking at 0°.

They are ubiquitously observed on the solar disk and off the solar limb exhibiting blue or red wing asymmetry in H$\alpha$, Ca II 854.2 nm, and Ca II K lines, reflecting continuous plasma upflows (Ø. Langangen et al. 2008; L. Rouppe van der Voort et al. 2009; S. Bose et al. 2019), which are thought to be driven by magnetic reconnection or wave processes (D. H. Sekse

Original content from this work may be used under the terms of the Creative Commons Attribution 4.0 licence. Any further distribution of this work must maintain attribution to the author(s) and the title of the work, journal citation and DOI.

et al. 2013a). D. H. Sekse et al. (2013b) also reported that the number of RREs detected near the disk center is half of that of the RBEs. This RRE/RBE ratio increases to 0.74 near the limb. They exhibit rapid decay, typically within a few seconds in chromospheric spectral lines without showing a descending pattern (D. H. Sekse et al. 2013a; V. Yurchyshyn et al. 2020), which is likely due to rapid heating to TR and coronal temperatures (e.g., L. Rouppe van der Voort et al. 2009).

It is worth noting that H. Wang et al. (1998) described a new type of small-scale chromospheric events, which they called upflows, and suggested that they may be fueling coronal heating. Authors argued that these events are due to magnetic reconnection between the existing network fields and opposite-polarity internetwork fields and ephemeral regions. J. Chae et al. (1998) attempted to associate these upflows with explosive events and magnetic reconnection observed in QS areas with the Solar Ultraviolet Measurements of Emitted Radiation instrument, while C.-Y. Lee et al. (2000) reported that the majority of the upflow events show absorption only in the blue wing of the H$\alpha$ line, which is similar to the RBEs (e.g., Ø. Langangen et al. 2008).

The formation mechanisms of solar spicules have been a subject of numerous observational and numerical studies. RBEs and RREs appear as jetlike features with Alfvénic velocities and may be the result of transverse pulses or disturbances propagating along magnetic flux tubes (D. Kuridze et al. 2015; S. Danilovic et al. 2023). Various data also indicate that they may be driven by small-scale magnetic reconnection events (e.g., V. Yurchyshyn et al. 2013, 2024; T. Samanta et al. 2019) in the chromosphere, where the interaction and rearrangement of magnetic field lines can release energy and drive plasma jets (T. Yokoyama & K. Shibata 1996). More recent high-resolution simulations have examined the complex interplay of convection, magnetic fields, and wave propagation in the lower solar atmosphere, suggesting that a combination of these processes might be responsible for the diverse properties of observed spicules (J. Martínez-Sykora et al. 2017).

Several studies were also focused on analyzing spectral properties of type II spicules, in particular, their chromospheric counterparts observed in Ca II 854.2 nm and H$\alpha$ 656.3 nm spectral lines, and increasingly in UV lines such as Mg II *h* and *k*, C II, and Si IV (e.g., L. Rouppe van der Voort et al. 2009; T. Samanta et al. 2019; S. Bose et al. 2021). These studies reveal large Doppler velocities, nonthermal line broadening, and evidence of transverse and torsional Alfvénic motions, pointing toward the presence of upward-propagating MHD waves (B. De Pontieu et al. 2007b; T. J. Okamoto & B. De Pontieu 2011). For instance, D. Kuridze et al. (2015) analyzed CRisp Imaging SpectroPolarimeter data from the 1 m Swedish Solar Telescope (G. B. Scharmer et al. 2003) and reported that high-speed (50–150 km s$^{-1}$) RREs and RBEs often originate from magnetic bright points exhibiting fast, nonlinear transverse motions (4–31 km s$^{-1}$) and short lifetimes (within a few seconds), suggesting rapid heating to coronal temperatures possibly driven by Kelvin–Helmholtz instability. S. Bose et al. (2021) reported a rich variety of H$\alpha$ profiles associated with RBEs and RREs, ranging from pure RBE-type profiles (only blueshift) to pure RRE profiles (only redshift) with combinations of blue- and redshifted profiles of various intensities. These authors argue that downflowing RREs often trace previously heated spicular plasma returning along the same loops, with associated Doppler shifts matching typical redshifts in TR. Recently N. Vilangot Nhalil et al. (2023) studied various parameters of RBEs using H$\alpha$ and Si IV spectral lines and suggested that all events have either single- or multithreaded nature. They found that most RBEs show enhanced Si IV emission with a secondary blueshifted component, indicating a connection between chromospheric dynamics and TR heating. S. Danilovic et al. (2023) studied RREs and RBEs by realistic 3D MHD simulations, showing that their spectral signatures arise from motions perpendicular to magnetic field lines, supporting an Alfvénic wave interpretation. On the other hand, spectral observations of RBEs and RREs off solar disks are scarce, and properties of off-disk profiles are not well explored. Off-disk spectra of type I spicules were intensively studied in the 1960s (e.g., J. B. Zirker 1962), and the contributions of many researchers were well summarized in a comprehensive review paper by J. M. Beckers (1968). More recently, H. Skogsrud et al. (2014) analyzed off-limb H$\alpha$ profiles identifying asymmetric double-peak profiles. Double-Gaussian fits revealed velocity differences of 20–30 km s$^{-1}$, consistent with internal flows, while spectral tilts suggested torsional motions, conforming models of chromospheric and coronal energy transport.

Here we present high-resolution on- and off-disk H$\alpha$ observations of small-scale dynamic features acquired with the Goode Solar Telescope (GST; W. Cao et al. 2010; P. R. Goode et al. 2010). Overall, there are many different spectral profiles, and most of them may be classified as RBEs, RREs, jets, or jetlike events. All of them show strong blue- or redshifted excursions, or various combinations of both. For the sake of brevity, and to disassociate ourselves from the terminology that might impose certain physical properties and/or origination mechanisms, here we will introduce and use a neutral term, rapid Doppler excursions (RDEs), which would indicate a feature with a notable line broadening. In cases when we cite results specifically derived for RBE or RRE events, we will use the original terminology used by the authors. Section 2 describes the observations and methods used in this study. In Section 3, we present the results of the analysis. In Section 4, we summarize and discuss our findings.

## 2. Data and Methods

In this study we used two different QS datasets. The first set (disk set) was acquired near the disk center on 2023 September 7 between 17:39 UT and 17:55 UT, and the second set (limb set) was collected at the solar limb (−590″,−700″) on 2024 August 4 between 18:40 UT and 18:42 UT. All data were observed with the aid of an adaptive optics system (S. Shumko et al. 2014).

The GST's Visible Imaging Spectrometer (VIS) acquired a series of narrowband H$\alpha$ images using a Fabry–Pérot interferometer with a bandpass of 0.008 nm and the permissibility to shift the bandpass by 0.02 nm around the H$\alpha$ line center. The pixel scale in this optical setup was 0.″029, and the field of view (FOV) of the imager was 75″ × 64″. To reduce possible temporal smearing, spectral scans were performed by rapidly switching the Fabry–Pérot interferometer between 13 predefined spectral positions using the following order: ±0.12, ±0.10, ±0.08, ±0.06, ±0.04, ±0.02, and 0.0 nm. The disk set was recorded with the time gap between two symmetrical spectral positions of about 2 s and the total scan duration of 25 s, while the time gap in the limb set was 1 s and the total

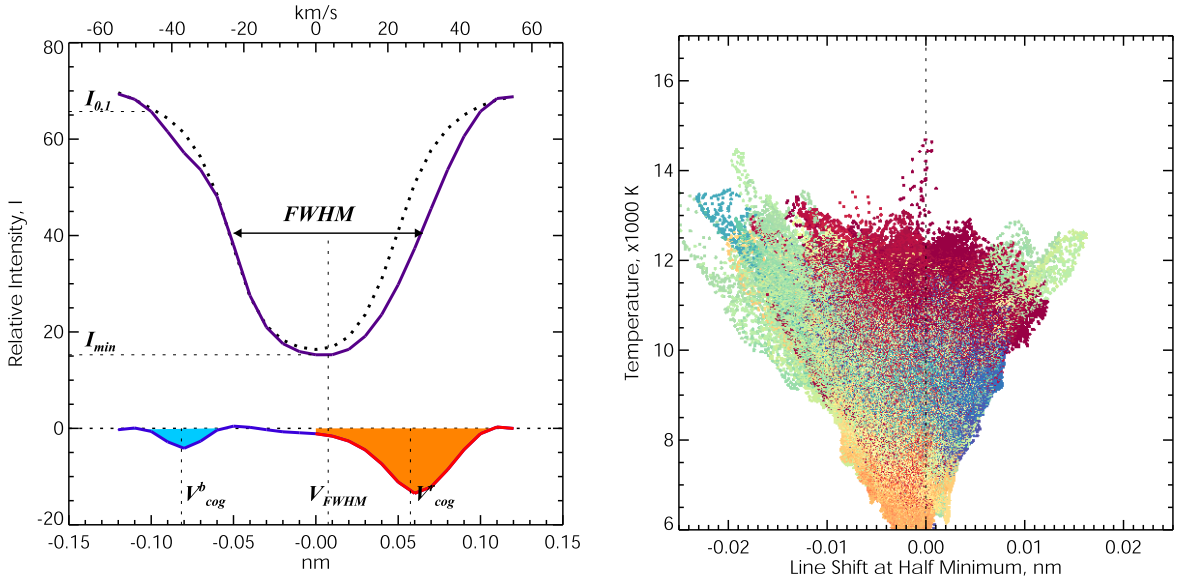


**Figure 1.** Left: a sample of an averaged H$\alpha$ 656.3 nm profile (dotted) overplotted with a randomly chosen spectral profile (purple) from the disk dataset. The blue–red curve at $I < 0$ is the corresponding CP. The blue/red shaded areas indicate locations where the total intensity of the CP and the COG velocities $V^b_{\rm COG}$ and $V^r_{\rm COG}$ (short vertical dotted lines) were calculated separately for each wing of the CP. Horizontal dotted lines at $I_{0.1}$ and $I_{\rm min}$ indicate intensity levels used to calculate the FWHM. The long vertical line indicates the corresponding Doppler shift, $V_{\rm FWHM}$. Right: chromospheric temperatures derived from the FWHM data plotted vs. the corresponding Doppler shift, $V_{\rm FWHM}$, measured using 40 spectral scans. Colors denote data points belonging to the same spectral scan.

scan duration was 12 s. At each spectral position we acquired a burst of 25 frames, and each burst was speckle reconstructed using the F. Wöger & O. von der Lühe (2007) speckle reconstruction technique to produce final images. The acquisition of bursts resulted in the lower data cadence; however, it gave us an advantage of higher spatial resolution. All 13 multiwavelength images within one scan were aligned among themselves and then aligned to all 40 scans of the observing period (X. Yang et al. 2022), thus generating a $(t, \lambda, x, y)$ data cube.

Using the disk dataset, an average QS profile was calculated for each spectral scan by averaging over the central $40'' \times 30''$ part of the FOV. We then calculated a ratio (correction curve) between the standard H$\alpha$ profile listed in the BASS2000 solar atlas[5] and the average QS profile. These correction curves were then applied to all spectral profiles in both datasets. Following the solar atlas by L. Delbouille et al. (1973), the intensity of each average profile was scaled between $I_{\rm min} = 17$ and $I_{0.1} = 65$ units, assuming the continuum intensity to be 100 units. Subsequently, each spectral profile in the datasets was scaled accordingly.

The left panel of Figure 1 shows an example of the corrected average QS profile from the disk set (dotted curve) overplotted with a randomly chosen data profile (purple) exhibiting asymmetric broadening. For each profile in the disk dataset we determined the full width of the profile at half-minimum (FWHM; horizontal arrow), calculated at half of the difference between the intensity at $\pm 0.1$ nm and the line minimum. The choice of this particular intensity range was defined by M. E. Molnar et al. (2019), who used the same range to determine the H$\alpha$ FWHM and compared it to the Atacama Large Millimeter/submillimeter Array (ALMA) temperature measurements. According to these authors, that range determines the width of the central core of the H$\alpha$ line, which is mainly formed in the chromosphere. The FWHM measurements also allowed us to determine the Doppler shift at that level as $V_{\rm FWHM} = (\Delta\lambda_b + \Delta\lambda_r)/2$, where $\Delta\lambda$ is the spectral offset from the line center to the corresponding half-minimum level (long vertical dashed line).

The blue–red curve in the left panel represents a contrast profile (CP) determined as the difference between the data and the average profiles. In this particular case, the CP shows two distinct minima since the data profile has broadening on the red side, as well as lower intensity in the range of $-0.06$ to $-0.11$ nm. Using CPs, determined for each data profile, we calculated the total blue and red wing CP intensities in the $-0.12 < \Delta\lambda < 0$ and $0 < \Delta\lambda < 0.12$ ranges (shaded areas), as well as the center-of-gravity (COG) speeds $V^b_{\rm COG}$ and $V^r_{\rm COG}$ (short vertical dotted lines).

## 3. Results

### 3.1. Thermal Properties of Small-scale On-disk Events

The full width of the H$\alpha$ line is known to be well correlated with the plasma temperature (J. Leenaarts et al. 2012; M. E. Molnar et al. 2019; L. A. Tarr et al. 2023). It should be noted that dynamic chromospheric features such as RBE/RREs may also exhibit nonthermal line broadening due to turbulence (e.g., H. Skogsrud et al. 2014), which is expected to produce symmetrical (insignificant Doppler shifts) broadened lines, indicating high temperatures without it being so. Moreover, wave-induced line broadening (D. Kuridze et al. 2015) and asymmetrical broadened profiles (J. Leenaarts et al. 2012) may lead to the temperature overestimation when applying the line width–temperature relationship. To convert FWHM measurements into chromospheric temperature, we used the empirical relationship $\mathrm{FWHM} = 0.553 + (6.12 \times 10^{-5})T$, derived by M. E. Molnar et al. (2019) by comparing H$\alpha$ and ALMA measurements. While the uncertainties in measuring FWHM and $T$ are very small (see Figure 4 in M. E. Molnar et al. 2019), the FWHM–$T$ has significant scatter, and the temperature can be estimated with an error of about $\pm 700$ K. This relationship is

[5] https://bass2000.obspm.fr/solar_spect.php

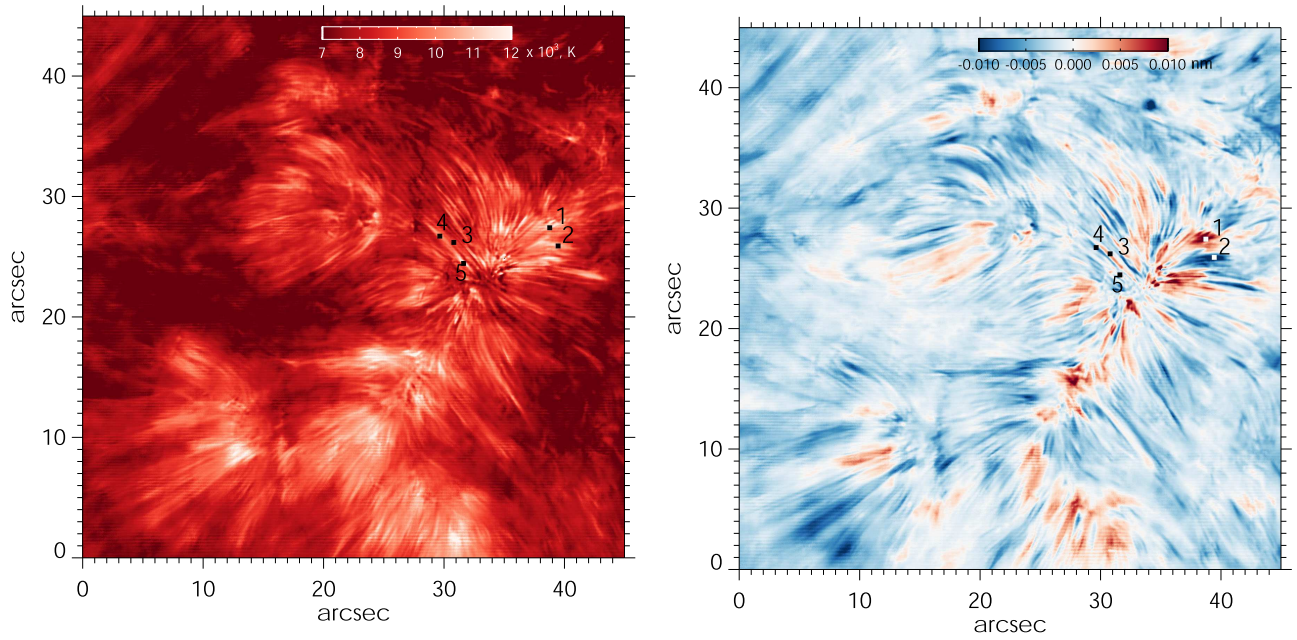


**Figure 2.** Left: temperature distribution derived from FWHM data scaled between 7000 and 12,000 K. Right: map of Doppler shifts derived as the spectral position of the midpoint measured at half-width and scaled between −0.01 and 0.01 nm.

dependent on any theoretical considerations and indicates that locations with broader H$\alpha$ line profiles tend to be associated with higher chromospheric temperatures. Nevertheless, the derived temperature distributions should be interpreted with caution, especially the numbers on the higher end of the temperature range. High-resolution spectroscopic data combined with sophisticated inversion tools are needed to untangle the complex relationship between the spectral line parameters and physical conditions in the chromosphere.

The right panel of Figure 1 plots the derived temperatures versus the corresponding Doppler shift, $V_{\rm FWHM}$. Data for each spectral scan are plotted using different colors. As expected, the large scatter of the data points indicates that there is no well-defined relationship between these two parameters. At the same time, the scatter plot shows two distinct asymmetries. First, it appears that blueshift dominates over weakly heated (6000–8000 K) features since the minimum of the $V_{\rm FWHM}$–$T$ relationship is centered at about −0.03 nm. Second, a distinct branch of data points suggests that strongly blueshifted ($<-0.01$ nm) chromospheric features tend to exhibit temperatures within the 9000–14,000 K range, while no strongly ($>0.01$ nm) redshifted features are detected at these temperatures. We note, however, that this branch of data points appears only in three line scans and should be considered as a suggestion of a possible asymmetry rather than solid observational evidence. Temperature (left) and Doppler shift $V_{\rm FWHM}$ (right) maps in Figure 2 show that indeed the majority of hot (>12,000 K, brightest in the temperature map) and cool (<9000 K; dark red) features are aligned with strongly and weakly blueshifted Doppler signals, which further illustrates the asymmetry in the temperature–Doppler shift plot and the predominance of data points in the $T < 8000$ K and $V_{\rm FWHM} < 0.0$ nm domain (see Figure 2).

The overwhelming majority of features exhibit temperature (line width) variation along their length such that the root and the tip of a spicule have lower temperature and the temperature gradually increases toward the midsection of the spicule. Depending on the nature of line broadening, this compact "hotter" region might indeed indicate higher plasma temperatures in this small localized region or the occurrence of significant heating possibly combined with both turbulent and jetlike flows. The data analyzed here do not allow us to disentangle these physical effects that might have contributed to the higher derived temperatures.

Frequency distributions of the derived Doppler shifts (left) and temperatures (right) are shown in Figure 3. The blueshifted pixels dominate; their distribution has a Gaussian-like shape with a cutoff with a maximum at ≈−0.02 nm, while the frequency distribution of the redshifted pixels resembles a wing of the Gaussian. One immediate concern that arises from this figure is that the blueshifted distribution might be due to instrumental effects such as errors in identifying the line center using a Fabry–Pérot interferometer. Careful inspection of line profiles showed that there is no systematic shift of the line center. Instead, the blueshift is due to the observed line asymmetry. The distribution of temperatures associated with blueshifted pixels is asymmetrical, with a peak in the low temperature range at 7200 K, and it gradually falls off toward the high temperature range, displaying a secondary maximum at about 8800 K. The redshifted pixels show a very different, nearly symmetrical distribution with a much lower amplitude that reaches maximum at about 9000 K. It appears that there is no significant difference between blue and red distribution for temperatures in the range $T > 10{,}000$ K, and the high-shift, high-temperature branch mentioned above has too few points to be prominent in the distribution.

In Figure 4, we show H$\alpha$ profiles associated with five distinct Doppler and temperature features marked in Figure 2. Features 1 and 2 are rather short ($\sim 3''$) and broad ($\sim 1''$) and resemble a typical chromospheric jet. Their spectral profiles are plotted in the left panel. Both exhibited a nearly similar magnitude of the Doppler shift and temperature, although the thermal structure of the redshifted Feature 1 appears to be finely structured, while the blueshifted Feature 2 seems to be associated with a relatively broad and uniform thermal signal.

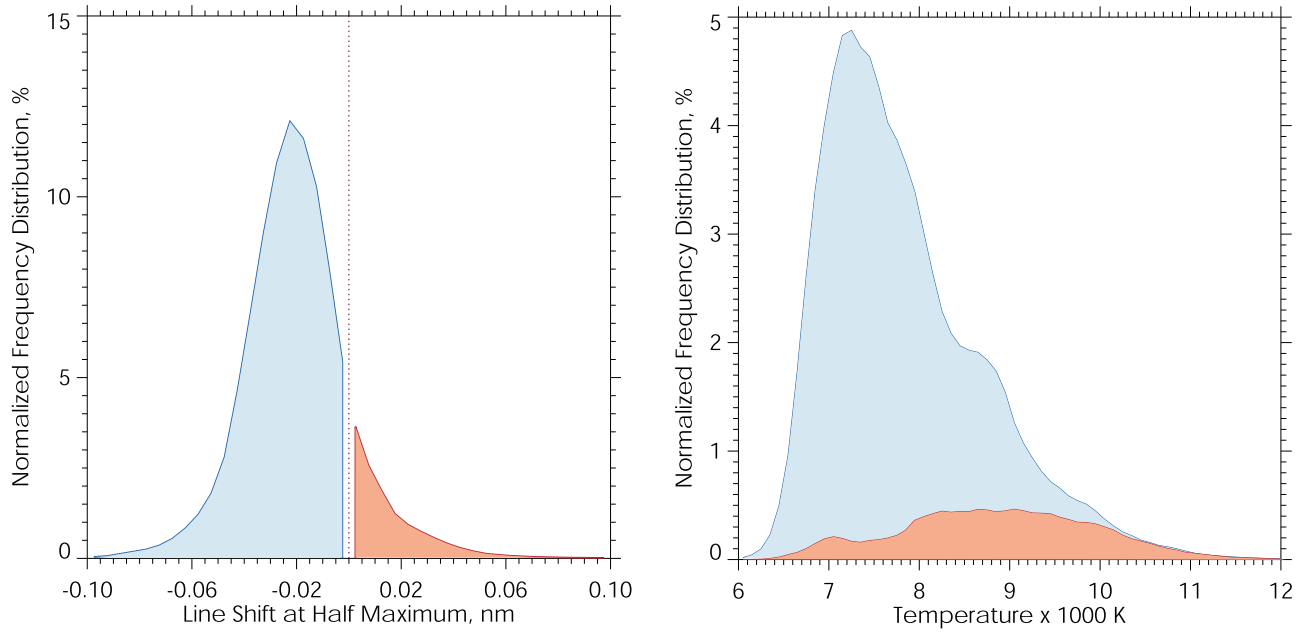


**Figure 3.** Frequency distribution of temperature and Doppler shifts plotted separately for blueshifted (light-blue shading) and redshifted (orange shading) pixels. The counts were normalized by the total number of blue- and redshifted pixels.

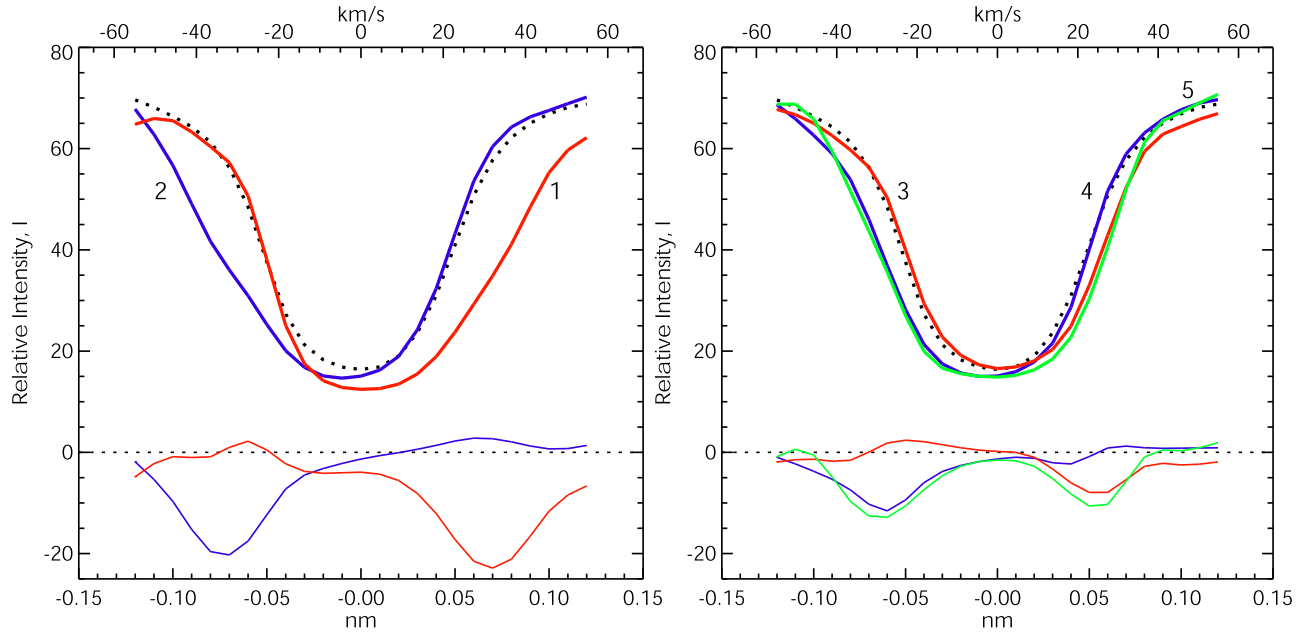


**Figure 4.** Spectral profiles at the five points marked in Figure 2. The left panel shows spectral profiles and CPs for Features 1 (blue) and 2 (red), while the right panel shows those for Features 3 (blue), 4 (red), and 5 (green).

The blue and red curves in the right panel of Figure 4 show spectra and CPs for Features 3 and 4, which visually resemble the well-known RBE and RRE spectra. Similarly, these profiles are broadened at one wing only, albeit in a different degree. Finally, the green curves are associated with the high-temperature and low Doppler shift Feature 5. The shapes of both spectra and CPs appear as if they are a superposition of the red and blue profiles. The maps in Figure 2 show that the redshifted Feature 4 displays significantly higher line broadening compared to that of the blueshifted Feature 3. All three features are closely positioned, and it is likely that Features 4 and 5 might belong to the large event, while Feature 3 is displaced from the RDE axis.

### 3.2. Spectral Properties of Off-disk RDEs

Figure 5 shows a sample of VIS data obtained on 2024 August 4 near the SE solar limb. Comparison of the H$\alpha$ blue ($-0.12$, $-0.1$, $-0.08$ nm) and red (0.12, 0.1, 0.08 nm) wing images indicates that there is a clear asymmetry: blueshifted events dominate the limb when observed in the far wings. It agrees with the data shown in the right panel of Figure 1, where blueshifted events display larger line shifts and higher temperatures. The orange and blue boxes in the top panel of Figure 5 outline the areas where we calculated average profiles shown in Figure 6. The orange box was placed in an area with a visibly low number of blueshifted features ("quiet" profile), while the blue box outlines an area with intense activity and a

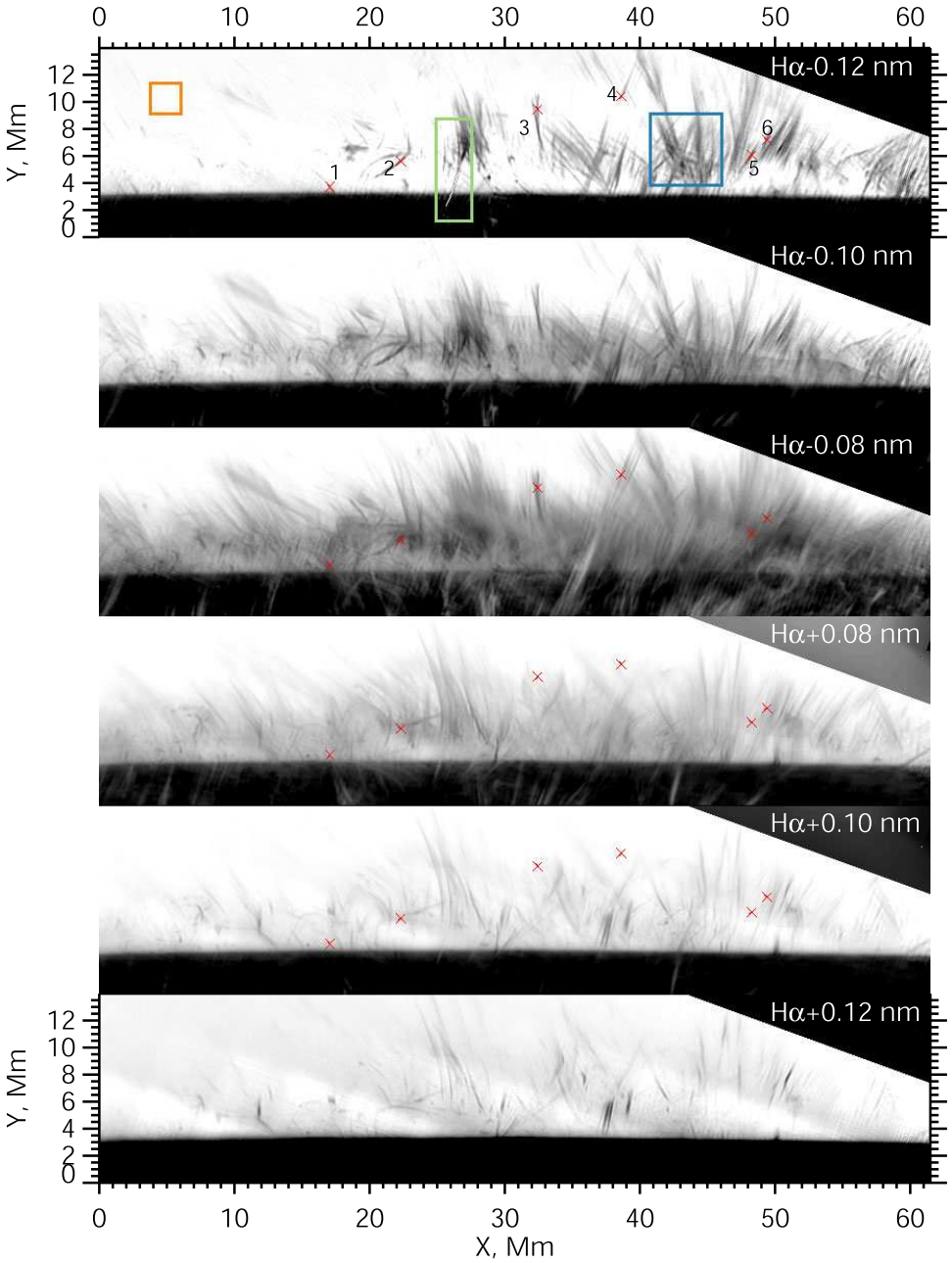


**Figure 5.** Limb activity as it appears in off-band H$\alpha$ images on 2024 August 4 at 18:40:16–18:40:26 UT using inverted colors. The edge of the solar disk is the dark segment at the bottom of each panel. The blue and orange squares outline an "intense" (blue) and a "quiet" (orange) area, respectively, where average profiles were calculated (see Figure 6).

large number of blueshifted features ("intense" profile). Both quiet and intense profiles in Figure 6 show asymmetric emission with a notable blueshift. In the case of the quiet profile the emission peaks at −0.02 nm, with a magnitude of ≈7 DN that is 14 times weaker than the continuum intensity at the disk center. In the case the intense profile, there are three distinct peaks with magnitudes of 18, 12, and 10 DN centered at −0.08, −0.03, and 0.07 nm, respectively.

Extensive search of published studies showed that there is a lack of information on the spectral properties of off-limb spicules and jets. For example, while T. M. D. Pereira et al. (2012) performed an extensive study of physical properties of spicules observed off the disk, no spectral properties were discussed in that publication. The only relevant data were found in H. Skogsrud et al. (2014, see Figure 3), where authors analyzed CRISP data obtained at the Swedish 1 m Solar Telescope, showing that several of the H$\alpha$ line profiles measured off the limb are asymmetrical, exhibiting two peaks positioned at either side of the H$\alpha$ line center. Single peak profiles presented in that study also peak at −0.02 nm and fall off at $\lambda > |0.05|$ nm.[6]

The green box in the top panel of Figure 5 outlines an RDE-like feature, the lower part of which is visible against the solar disk and the upper part of which is seen above the limb. This RDE event was short-lived (10–30 s), as it appeared only in two consecutive frames taken at a 10 s interval. Figure 7 shows variations of the H$\alpha$ line profiles along the spine of the RDE

[6] See also Figure 4.9 in H. Skogsrud (2011).

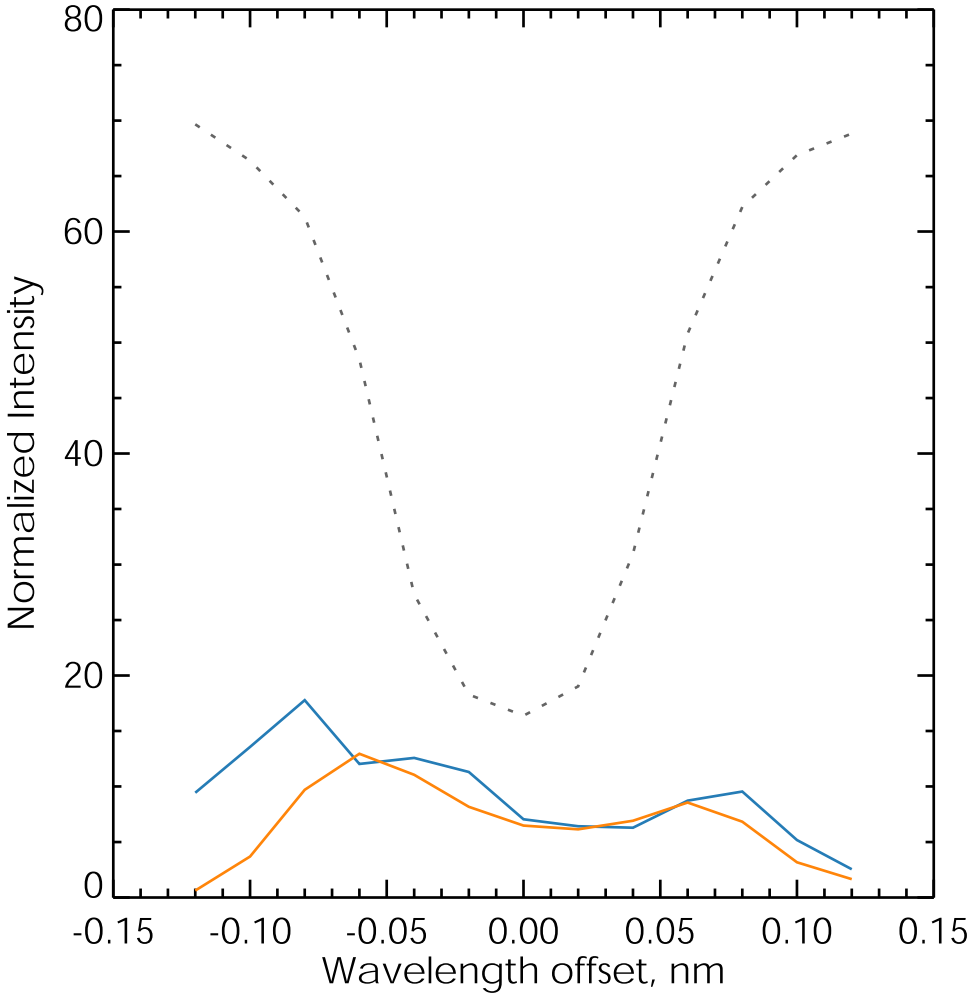


**Figure 6.** Blue and orange curves represent emission profiles averaged over areas outlined by the blue and orange boxes in the top panel of Figure 5. The dotted curve represents an average QS absorption profile measured at the disk center.

(color curves), as well as between two time steps (left and right panels).

When considering time evolution, the profiles remained largely unchanged. The most notable change occurred at $|\lambda| > 0.10$ nm within the lower (disk) part of the event, where far wings of the blue profiles turned upward approaching the shape of the average profile (dotted line). The purple dashed–dotted line in each plot represents a difference between profiles measured at the first point of the event (origin; dark-blue curve and circle in the inset) and its last point (tip; brown curve and circle in the inset). Both dashed–dotted lines appear nearly identical, indicating negligible changes in the RDE properties within a 12 s time interval.

When considering changes of the line profile along the spine of the feature, one change is prominent: as we move from the disk to the off-limb positions (i.e., from blue to red profiles), intensity decreases very rapidly at spectral ranges $|\lambda| > 0.05$ nm, revealing a "true" profile of the RDE. This suggests that in general RDE profiles observed against the solar disk are significantly affected by background radiation.

In Figure 8 we plot six H$\alpha$ single-pixel profiles measured at locations marked with crosses and digits in Figure 5. All six pixels belong to prominent and isolated H$\alpha-0.12$ nm chromospheric features. The selection criteria were as follows: the six pixels should belong to a single event and should not be overlapped by other H$\alpha-0.12$ nm features. Since the locations were selected using H$\alpha-0.12$ nm images, all these profiles show enhanced one- or two-peak emission at the far blue wing of the H$\alpha$ line. Their shape and amplitude appear to change depending on the height of the sampled pixel. For instance, profiles 1 and 2 (dark blue and light blue) that represent pixels closest to the photosphere (below 6 Mm) show intense single-peak emission in both blue and red wings. The blueshifted single peak now appears to be split into two peaks in profiles 5 and 6, sampled within the 6–8 Mm range, with the maxima at 0.08 and 0.04 nm. Finally, profiles 3 and 4, which sample pixels located above 8 Mm, exhibit a well-pronounced broad double peak in the 0.02–0.08 nm range, while no significant emission is observed in the red wing. In the right panel of Figure 8 we plot the height dependence of the averaged H$\alpha$ $-0.06$ nm (blue) and H$\alpha+0.06$ nm (red) intensities with height. The averaging was performed over the entire FOV (excluding the upper right corner with missing data) shown in Figure 5. The data shown in this plot are consistent with the idea of the predominance of the blueshifted plasma in the solar chromosphere observed off the solar disk (marked by the vertical dotted line at $x = 0$ Mm). At heights $> 0$ Mm both intensities fall off sharply; however, the drop in H$\alpha-0.06$ nm is only about 40% from its initial level of 28 DN, while the H$\alpha$ $+0.06$ nm intensity decreased by about 60%. This difference

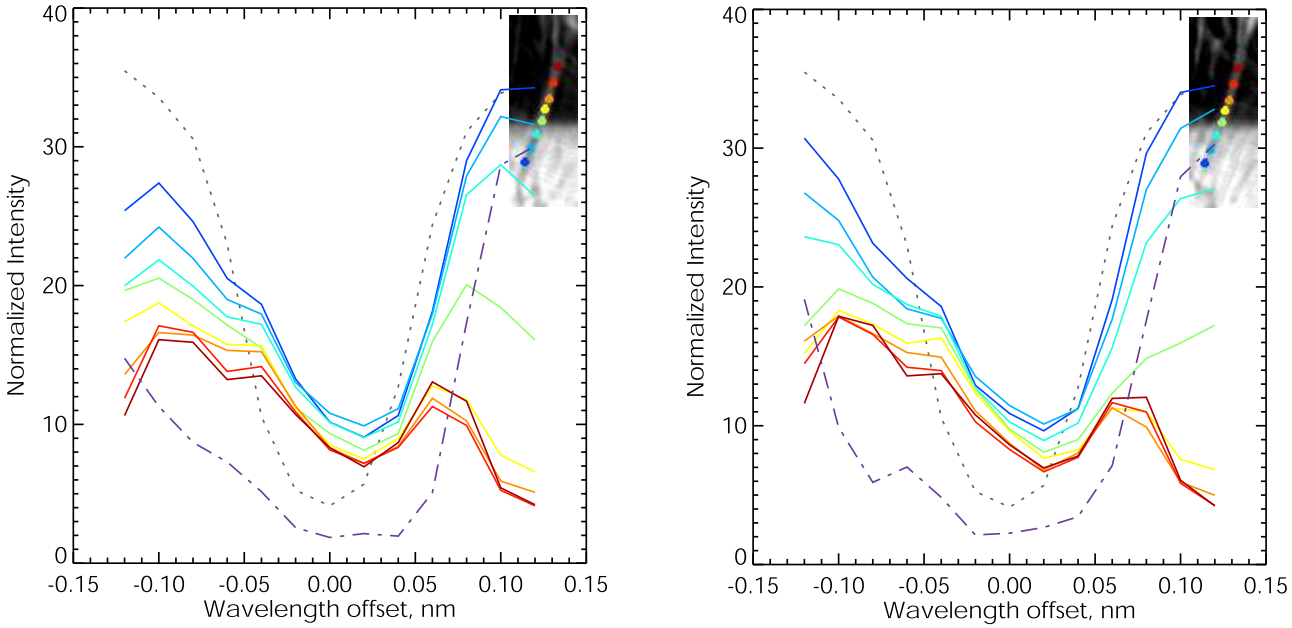


**Figure 7.** Variations of the H$\alpha$ line profile along the spine of the RDE event as measured at 18:40:04–18:40:14 UT (left) and 18:40:16–18:40:26 UT (right). The inset in the upper right corner zooms in on the RDE event outlined with a green box in the top panel of Figure 5. The color of each profile indicates the position along the RDE spine (inset) where it was measured. The thin dotted curve is a rescaled version of the QS absorption profile measured at the disk center. The purple dashed–dotted curve is the difference between the dark-blue disk profile (root of the RDE) and the brown limb (tip of the RDE) profile. Note that the line profiles in this plot were not shifted in the $y$-direction.

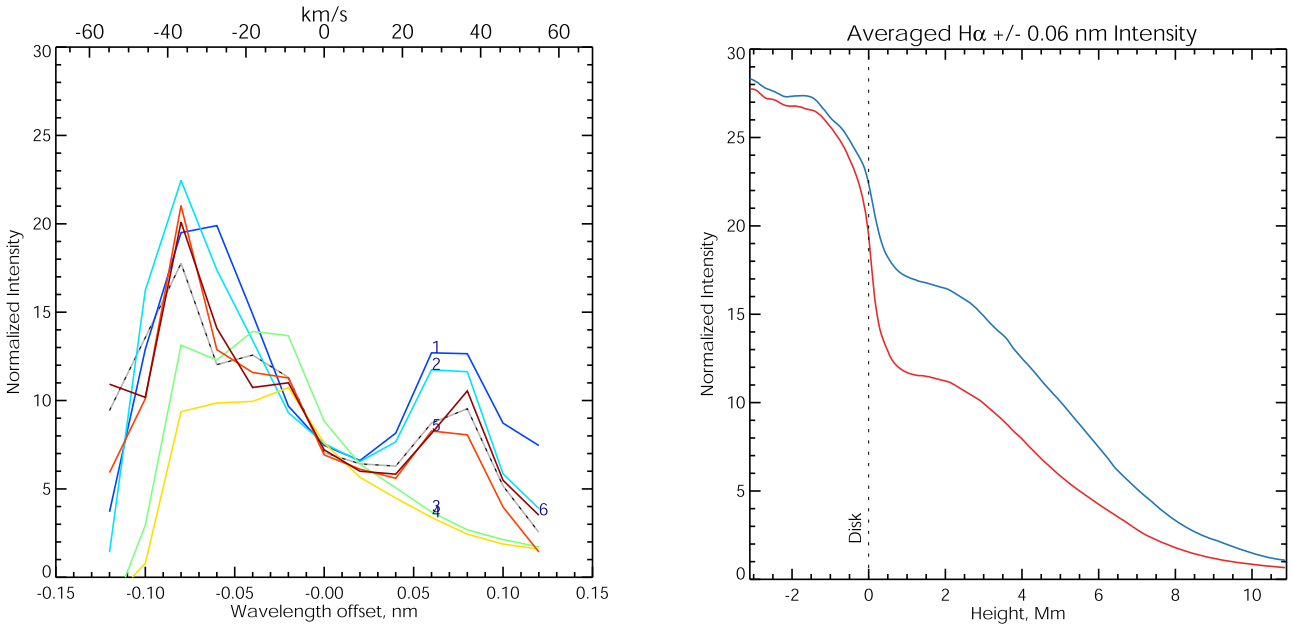


**Figure 8.** Left: H$\alpha$ line profiles plotted for six well-defined off-limb features marked in Figure 5 by crosses and digits. The black–gray dotted line is the averaged "intense" profile shown in Figure 6. The inset shows variations of H$\alpha$+0.06 nm (red) and H$\alpha$−0.06 nm (blue) depending on the height above the photosphere. Right: variations of averaged H$\alpha$−0.06 nm (blue) and H$\alpha$+0.06 nm (red) with height. The dotted line indicates the position of the solar limb.

gradually diminishes and becomes negligible at heights exceeding 10 Mm above the limb.

We used a combination (green curve in Figure 9) of four Gaussians (dotted curves) to approximate the mean off-limb RDE profile (red curve and symbols) calculated by averaging four off-limb RDE profiles (yellow, orange, red, and brown) shown in the right panel of Figure 7. The four Gaussians were found to be centered at −0.10, −0.04, 0.01, and 0.07 nm off the H$\alpha$ line center. All but Gaussian 4 have a similar $\sigma$ value of about 0.025 nm. The four-Gaussian fit highlights the fact that an RDE profile possibly results from contributions of different plasma streams. It appears that there might be a nearly equal contribution from red- and blueshifted plasma with velocities ranging from 10 to 40 km s$^{-1}$ (Gaussian 2 and 4). The weakest contribution (Gaussian 3) comes from weakly blueshifted plasma with velocities peaking at about 5 km s$^{-1}$. Note that the typical observable rate of transverse displacement of RBEs and RREs is in the range of 7−15 km s$^{-1}$ (see Figure 3 in B. De Pontieu et al. 2007b; D. Kuridze et al. 2015, and references therein). Finally, Gaussian 1 suggests the presence of much

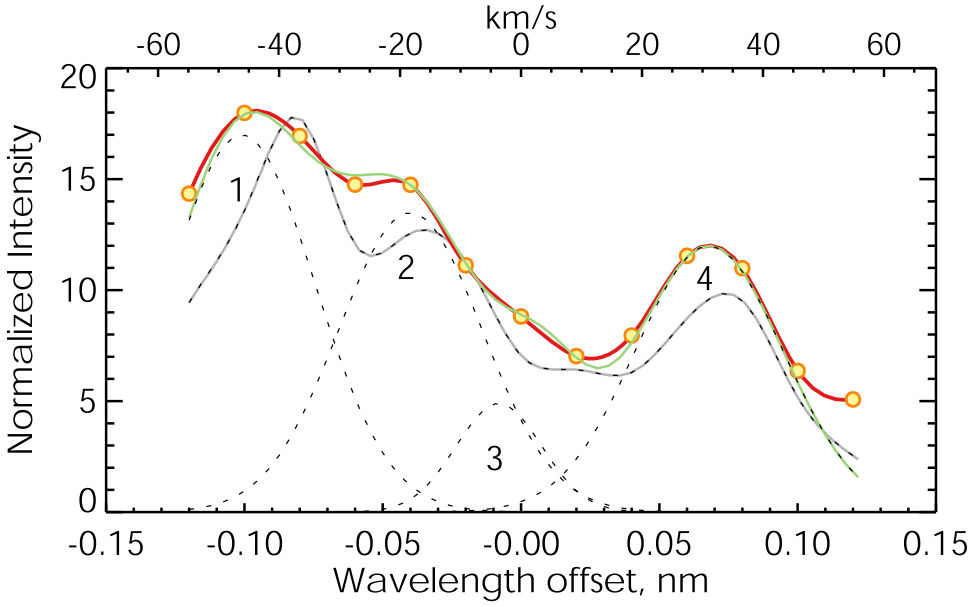


**Figure 9.** Red curve with circles: mean limb profile of the studied RDE reinterpolated for smoothness. Black–gray dotted curve: average "intense" H$\alpha$ profile shown as a blue curve in Figure 6. Green: sum of four Gaussian curves plotted with dotted lines.

stronger flows with velocities in excess of 30 km s$^{-1}$ and reaching about 60 km s$^{-1}$. Figure 5 shows that spicules tend to be inclined toward the surface. Observed nearly vertical features might be inclined as well, but in the line-of-sight (LOS) direction. Assuming that the observed LOS velocities are components of the field-aligned flows and accepting an inclination angle of 45°, we obtain 45–90 km s$^{-1}$ flows along the axis of a spicule, which is within the velocity range reported for on-disk spicules (50–150 km s$^{-1}$; e.g., B. De Pontieu et al. 2007a).

The overplotted gray dotted curve in Figure 9 is the averaged "intense" profile shown in Figure 6. Although there is a nonnegligible difference between the mean off-limb RDE profile (red) and the average "intense" profile, their overall shape is quite similar. As with the mean RDE profile, the "intense" profile displays the same three well-defined components centered at −0.08, −0.03, and 0.075 nm. This similarity suggests that the RDE profiles shown in Figures 7 and 9 might be contaminated by contributions from various small-scale features along the LOS, such as oscillating spicules and high-speed jetlike spicules.

## 4. Summary and Discussion

Double-peaked RBE and RRE profiles are often interpreted as signatures of bidirectional flows, torsional motions (L. Rouppe van der Voort et al. 2009; B. De Pontieu et al. 2012; D. H. Sekse et al. 2012), shocks, and shock-driven plasma (e.g., J. Chae et al. 2014) and may be significantly influenced by radiative transfer effects under dynamic, non-LTE conditions (J. Leenaarts et al. 2012). Figure 2 in S. Bose et al. (2021) presents a large variety of H$\alpha$ profiles measured on the disk that display single- and two-peaked structures. These double-peaked events consist of one blueshifted peak and one redshifted peak of various intensities. However, none of the presented profiles show two or more blue- or redshifted peaks. H. Skogsrud et al. (2014) presented several H$\alpha$ spicule profiles, measured off-disk, exhibiting a similar double-peaked structure with prominent redshifted peaks centered within a +30 to +50 km s$^{-1}$ range. In contrast, this study features off-disk H$\alpha$ profiles that exhibit a complex and asymmetric three-peak morphology. We closely inspected profiles of six isolated features, and in all of them we detected at least two well-pronounced blueshifted emission peaks and a redshifted peak. These multipeak profiles of thin chromospheric features observed at the limb have not been reported before. The persistent presence of peaks within specific wavelength ranges, coupled with enhanced blue wing emission, may indicate the existence of intricate velocity fields along the LOS. However, the similarity between the spatially averaged "intense" off-disk profile and single-pixel spectra poses a critical question: does the observed multipeak structure arise from the complex velocity field within a single event, or does it result from the LOS integration? The similarity of profiles measured along the spine of an RDE (Figure 7) seems to support the single-event interpretation since it is reasonable to expect that the result of the LOS integration would be highly variable as we move along an RDE from the root to the tip. Another argument in favor of the single-event interpretation is the fact that four out of six single-pixel profiles in Figure 8 exhibit blueshifted double-peaked emission structure. It is better pronounced in profiles 3 and 4, which are expected to be less affected by (but not free of) LOS integration effects since they represent pixels located at heights exceeding 9 Mm above the majority of chromospheric structures and sample tips of RDEs. In contrast, in profiles 1 and 2 the blueshifted double-peak structure appears as one broad peak, possibly suggesting that it results from overlapping many single- and double-peaked structures during the LOS integration (see also H. Skogsrud et al. 2014). It is therefore likely that the blueshifted double-peaked structure does not fully result from LOS integration but may also reflect a complex velocity field within a single event. However, it is not clear to what degree these profiles are affected by LOS integration, and future studies of the subject would greatly benefit from multiwavelength datasets. Consequently, precautions should be taken when interpreting a single-pixel on-disk or off-disk RDE spectrum since it may not be arising from an isolated velocity component. Instead, it may

incorporate contributions from multiple dynamic structures along the LOS, potentially explaining the rich variety of observed RDE profiles as discussed, e.g., in H. Skogsrud et al. (2014), S. Bose et al. (2021), and N. Vilangot Nhalil et al. (2023).

Across both on-disk and off-disk observations, a consistent trend is the predominance of blueshifted plasma. On-disk Dopplergrams measured near the H$\alpha$ line core in this study reveal widespread blueshifts across the FOV, often linked to hotter, upward-moving plasma (L. Rouppe van der Voort et al. 2009). In contrast, redshifts appear to be more spatially localized: typically near network magnetic elements (see also Figure 4 in V. Yurchyshyn et al. 2024). This inference is somewhat misaligned with D. H. Sekse et al. (2013b), who reported that RBEs and RREs are similarly distributed and occur at the same spatial locations. Moreover, the red wing component seems to diminish more rapidly with height as compared to the blue component, which indicates that while blueshifted upflows extend to higher altitudes, redshifted emission might be associated with downflows or lower-atmospheric velocity components confined to network lanes, potentially representing return flows or draining of post-heated loops (e.g., B. De Pontieu et al. 2011). The aforementioned differences in spatial distribution of RBEs and RREs may further imply that RBEs and RREs are not similar phenomena; the associated flows may have different origins.

This H$\alpha$ line asymmetry and the chromospheric upflows they indicate well align with findings that selected UV spectral lines observed in the TR above network regions and show significant asymmetry in the blue wing, indicating the presence of high-velocity upflows (S. W. McIntosh & B. De Pontieu 2009). These authors interpreted the TR upflows as a manifestation of the mass transport between the chromosphere and the corona. B. De Pontieu et al. (2009) reported instances when chromospheric spicules were associated with coronal upflows, thus suggesting that spicules, as well as other small-scale high speed events, may play a significant role in the mass transport cycle that supplies the corona with hot plasma.

The ubiquitous presence of high LOS velocities of 30–60 km s$^{-1}$ observed off the disk (see also T. M. D. Pereira et al. 2012) in the $-0.1$ to $-0.08$ nm range aligns well with findings based on MHD modeling (S. Danilovic et al. 2023) showing that the vertical velocity component is always associated with a similar magnitude velocity component, perpendicular to the magnetic field line. In addition, J. Chae et al. (2024) reported on large-amplitude (up to 2 Mm) transverse MHD waves that exhibit a mean velocity amplitude of 25 km s$^{-1}$ and a mean period of 5.8 minutes, while the presence of strong turbulent flows within a spicule was reported by H. Skogsrud et al. (2014). These data support the idea that observed RDEs could be manifestations of Alfvén waves (D. H. Sekse et al. 2013a; R. Sharma et al. 2017) generated by various processes such as new flux emergence (e.g., H. Isobe et al. 2008; A. A. van Ballegooijen et al. 2011; A. K. Srivastava et al. 2017), vigorous turbulent flows (e.g., M. J. Aschwanden et al. 2018; J. Liu et al. 2019), or magnetic reconnection (e.g., H. Isobe et al. 2008). However, it is not obvious why long-period oscillations (order of several minutes) with large transverse velocities produce very short-lived (order of tens of seconds; e.g., T. M. D. Pereira et al. 2012; D. H. Sekse et al. 2013a) RDEs. It is also not clear what, in this case, drives the rapid RBE evolution, which includes various splitting patterns (V. Yurchyshyn et al. 2020).

Disk-to-off-limb variations in H$\alpha$ profiles offer additional insight into the structural and radiative properties of small-scale chromospheric features. A pronounced decrease in far-wing intensity (offsets $>0.05$ nm) as RDEs extend from the disk onto the off-limb indicates a change in the dominant source of wing emission. This change likely reflects evolving optical depth conditions as features rise above the optically thick lower atmosphere. The relative constancy of wing intensities along the off-disk portion suggests that the physical parameters of the emitting plasma, such as temperature and velocity dispersion, remain relatively stable along the observed spine of the feature.

The frequency distribution of temperatures associated with blueshifted pixels seems to be composed of two components centered at 7200 and 8800 K. The cooler 7200 K component is primarily found in the areas away from the network fields, while the hotter 8800 K component is associated with larger Doppler shifts and RDEs originating from the network fields. It should be noted that our finding is supported by L. A. Tarr et al. (2023), who reported a bimodal distribution of ALMA brightness temperatures, with the higher temperatures associated with network fields and short-lived dynamics features. The temperature distribution of the redshifted pixels display a very gradual increase and decrease with a maximum at approximately the same temperature as the blueshifted hot component, suggesting that redshifted plasma may either represent downflows of previously heated plasma or be a product of the same heating mechanism that is responsible for energizing the blueshifted plasma.

To summarize, we outline below the main findings of this study:

(1) Off-disk H$\alpha$ emission profiles show an asymmetrical three-peak structure within the dominant blue wing part of the H$\alpha$ line. The maximum of the peaks is centered within $-0.01$ to $-0.08$ nm, $-0.07$ to $-0.03$ nm, and 0.04–0.09 nm spectral ranges.
(2) The similarity between the averaged off-disk and single-pixel profiles seems to suggest that an RDE spectrum, measured at a single pixel, may include contributions from other dynamic features along the LOS. The data also suggest that the LOS integration may be more significant within a 6 Mm layer above the photosphere.
(3) The bimodal frequency distribution of chromospheric temperatures associated with blueshifted features indicates that some locations may either be strongly heated or exhibit significant turbulent motions and nonthermal line broadening. Those locations mainly correspond to the central parts of blue- and redshifted chromospheric features.

To confirm the existence of the multipeak structures detected in the blue wing of the H$\alpha$ line and understand their origin, as well as the cause for the bimodal temperature distribution, further off-disk multiwavelength spectral observations are needed. In particular, high spatial (of order of 0.″1) and temporal ($<1$ s) observations of limb RDEs may further unveil details of their origin, as well as morphological and temporal evolution. The new off-limb adaptive optic system *Cona* (D. Schmidt et al. 2025) recently implemented at the Big Bear Solar Observatory will be instrumental for this effort. However, to fully understand the complex line profiles possibly arising from the interplay between field-line-directed

plasma flows, RDE oscillations, and twisting and turbulent motions, non-LTE inversion routines should be applied to high-quality spectral data.

## Acknowledgments

We thank the anonymous referee for many critical comments and suggestions that allowed us to improve the paper. We acknowledge the use of data from the Goode Solar Telescope (GST) of the Big Bear Solar Observatory (BBSO). BBSO operation is supported by the US NSF AGS 2309939 grant and the New Jersey Institute of Technology. The GST operation is partly supported by the Korea Astronomy and Space Science Institute and the Seoul National University. E.-K.L. was supported by the Korea Astronomy and Space Science Institute under the R&D program of the Korean government (MSIT; No. 2025-1-850-02). V.Y. acknowledges the support from US NSF AGS grants 2300341, 2408174, and 2401229; NSF grant AST-2108235; and NASA grant 80NSSC24K1914.

*Facility:* GST.

## ORCID iDs

Vasyl Yurchyshyn https://orcid.org/0000-0001-9982-2175
Seray Şahin https://orcid.org/0000-0003-3469-236X
Eun-Kyung Lim https://orcid.org/0000-0002-7358-9827
Xu Yang https://orcid.org/0000-0002-3238-0779
Wenda Cao https://orcid.org/0000-0003-2427-6047

## References

Aschwanden, M. J., Gošic, M., Hurlburt, N. E., & Scullion, E. 2018, ApJ, 866, 73
Beckers, J. M. 1968, SoPh, 3, 367
Bose, S., Henriques, V. M. J., Joshi, J., & Rouppe van der Voort, L. 2019, A&A, 631, L5
Bose, S., Joshi, J., Henriques, V. M. J., & Rouppe van der Voort, L. 2021, A&A, 647, A147
Bose, S., Joshi, J., Testa, P., & De Pontieu, B. 2025, ApJL, 983, L7
Cao, W., Gorceix, N., Coulter, R., et al. 2010, AN, 331, 636
Chae, J., van Noort, M., Madjarska, M. S., et al. 2024, A&A, 687, A249
Chae, J., Wang, H., Lee, C.-Y., Goode, P. R., & Schühle, U. 1998, ApJL, 504, L123
Chae, J., Yang, H., Park, H., et al. 2014, ApJ, 789, 108
Danilovic, S., Bjørgen, J. P., Leenaarts, J., & Rempel, M. 2023, A&A, 670, A50
De Pontieu, B., Carlsson, M., Rouppe van der Voort, L. H. M., et al. 2012, ApJL, 752, L12
De Pontieu, B., Erdélyi, R., & James, S. P. 2004, Natur, 430, 536
De Pontieu, B., McIntosh, S., Hansteen, V. H., et al. 2007a, PASJ, 59, 655
De Pontieu, B., McIntosh, S. W., Carlsson, M., et al. 2007b, Sci, 318, 1574
De Pontieu, B., McIntosh, S. W., Carlsson, M., et al. 2011, Sci, 331, 55
De Pontieu, B., McIntosh, S. W., Hansteen, V. H., & Schrijver, C. J. 2009, ApJL, 701, L1
Delbouille, L., Roland, G., & Neven, L. 1973, Atlas Photometrique du Spectre Solaire de λ 3000 a λ 10000 (Universite de Liege, Institut d'Astrophysique)
Goode, P. R., Coulter, R., Gorceix, N., Yurchyshyn, V., & Cao, W. 2010, AN, 331, 620
Hansteen, V. H., De Pontieu, B., Rouppe van der Voort, L., van Noort, M., & Carlsson, M. 2006, ApJL, 647, L73
Henriques, V. M. J., Kuridze, D., Mathioudakis, M., & Keenan, F. P. 2016, ApJ, 820, 124
Herde, V. L., Chamberlin, P. C., Schmit, D., et al. 2023, ApJ, 946, 103
Isobe, H., Proctor, M. R. E., & Weiss, N. O. 2008, ApJL, 679, L57
Kuridze, D., Henriques, V., Mathioudakis, M., et al. 2015, ApJ, 802, 26
Langangen, Ø., De Pontieu, B., Carlsson, M., et al. 2008, ApJL, 679, L167
Lee, C.-Y., Chae, J., & Wang, H. 2000, ApJ, 545, 1124
Leenaarts, J., Carlsson, M., & van der Voort, L. R. 2012, ApJ, 749, 136
Liu, J., Nelson, C., Snow, B., Wang, Y., & Erdélyi, R. 2019, NatCo, 10, 3504
Martínez-Sykora, J., De Pontieu, B., Hansteen, V. H., et al. 2017, Sci, 356, 1269
McIntosh, S. W., & De Pontieu, B. 2009, ApJ, 707, 524
McIntosh, S. W., De Pontieu, B., Carlsson, M., et al. 2011, Natur, 475, 477
Molnar, M. E., Reardon, K. P., Chai, Y., et al. 2019, ApJ, 881, 99
Narang, N., Arbacher, R. T., Tian, H., et al. 2016, SoPh, 291, 1129
Okamoto, T. J., & De Pontieu, B. 2011, ApJL, 736, L24
Pereira, T. M. D., De Pontieu, B., & Carlsson, M. 2012, ApJ, 759, 18
Pereira, T. M. D., De Pontieu, B., Carlsson, M., et al. 2014, ApJL, 792, L15
Rouppe van der Voort, L., De Pontieu, B., Pereira, T. M. D., Carlsson, M., & Hansteen, V. 2015, ApJL, 799, L3
Rouppe van der Voort, L., Leenaarts, J., De Pontieu, B., Carlsson, M., & Vissers, G. 2009, ApJ, 705, 272
Samanta, T., Tian, H., Yurchyshyn, V., et al. 2019, Sci, 366, 890
Scharmer, G. B., Bjelksjo, K., Korhonen, T. K., Lindberg, B., & Petterson, B. 2003, SPIE, 4853, 341
Schmidt, D., Schad, T. A., Yurchyshyn, V., et al. 2025, NatAs, 9, 1148
Sekse, D. H., Rouppe van der Voort, L., & De Pontieu, B. 2013a, ApJ, 764, 164
Sekse, D. H., Rouppe van der Voort, L., De Pontieu, B., & Scullion, E. 2013b, ApJ, 769, 44
Sekse, D. H., van der Voort, L. R., & Pontieu, B. D. 2012, ApJ, 752, 108
Sharma, R., Verth, G., & Erdélyi, R. 2017, ApJ, 840, 96
Shumko, S., Gorceix, N., Choi, S., et al. 2014, SPIE, 9148, 914835
Skogsrud, H., Rouppe van der Voort, L., & De Pontieu, B. 2014, ApJL, 795, L23
Srivastava, A. K., Shetye, J., Murawski, K., et al. 2017, NatSR, 7, 43147
Skogsrud, H. 2011, MA thesis, Univ. of Oslo http://urn.nb.no/URN:NBN:no-28837
Tarr, L. A., Kobelski, A. R., Jaeggli, S. A., et al. 2023, FrASS, 9, 436
Tian, H., DeLuca, E. E., Cranmer, S. R., et al. 2014, Sci, 346, 1255711
van Ballegooijen, A. A., Asgari-Targhi, M., Cranmer, S. R., & DeLuca, E. E. 2011, ApJ, 736, 3
Vilangot Nhalil, N., Shetye, J., & Doyle, J. G. 2023, MNRAS, 524, 1156
Wang, H., Johannesson, A., Stage, M., Lee, C., & Zirin, H. 1998, SoPh, 178, 55
Wöger, F., & von der Lühe, O. 2007, ApOpt, 46, 8015
Yang, X., Cao, W., & Yurchyshyn, V. 2022, ApJS, 262, 55
Yokoyama, T., & Shibata, K. 1996, PASJ, 48, 353
Yurchyshyn, V., Abramenko, V., & Goode, P. 2013, ApJ, 767, 17
Yurchyshyn, V., Cao, W., Abramenko, V., Yang, X., & Cho, K.-S. 2020, ApJL, 891, L21
Yurchyshyn, V., Schmidt, A., Wang, J., et al. 2024, ApJ, 961, 79
Zirker, J. B. 1962, ApJ, 136, 250